Structure of the yeast ribonucleotide reductase Y2Y4 heterodimer

Walter C. Voegtli*, Jie Ge†, Deborah L. Perlstein†, JoAnne Stubbe†, and Amy C. Rosenzweig*‡

*Departments of Biochemistry, Molecular Biology, and Cell Biology and of Chemistry, Northwestern University, Evanston, IL 60208; and †Departments of Chemistry and of Biology, Massachusetts Institute of Technology, Cambridge, MA 02139

Contributed by JoAnne Stubbe, July 2, 2001

The R2 subunits of class I ribonucleotide reductases (RNRs) house a diferric-tyrosyl radical (Y·) cofactor essential for DNA synthesis. In yeast, there are two R2 proteins, Y2 and Y4. Although both Y2 and Y4 are homologous to R2s from other organisms, Y4 lacks three conserved iron-binding residues, and its exact function is unclear. Y4 is required for assembly of the diferric-Y· cofactor in Y2, and the two proteins can form both homodimeric and heterodimeric complexes. The Y2Y4 heterodimer was crystallized from a mixture of the two proteins, and its structure was determined to 2.8 Å resolution. Both Y2 and Y4 are completely α helical and resemble the mouse and *Escherichia coli* R2s in overall fold. Three α helices not observed in the mouse R2 structure are present at the Y2 N terminus, and one extra N-terminal helix is observed in Y4. In addition, one of the eight principal helices in both Y2 and Y4, αD, is shifted significantly from its position in mouse R2. The heterodimer interface is similar to the mouse R2 homodimer interface in size and interacting residues, but loop regions at the interface edges differ. A single metal ion, assigned as Zn(II), occupies the Fe2 position in the Y2 active site. Treatment of the crystals with Fe(II) results in difference electron density consistent with formation of a diiron center. No metal-binding site is observed in Y4. Instead, the residues in the active site region form a hydrogen-bonding network involving an arginine, two glutamic acids, and a water molecule.

Ribonucleotide reductases (RNRs) catalyze the reduction of ribonucleotides to the corresponding deoxyribonucleotides, an essential step in nucleotide metabolism in all organisms (1). By providing a balanced pool of monomeric precursors for DNA replication and repair, these enzymes play a crucial role in control of cell proliferation. Members of the largest class of RNRs, class I, are found in all eukaryotes, in many prokaryotes, and in several viruses. The catalytically active form of class I RNRs is proposed to be an $\alpha_2\beta_2$ tetramer (2). The homodimeric α subunit, called R1, houses the active site and binding sites for allosteric effectors. The β subunit, called R2, contains a diiron cluster that in its reduced state reacts with dioxygen to form a stable tyrosyl radical (Y·) and a diiron(III) cluster. This essential Y· is proposed to generate a thiyl radical, located on a cysteine residue in the R1 active site, that initiates ribonucleotide reduction (3, 4).

The most extensively characterized class I RNR system is that found in *Escherichia coli*. Crystal structures of both the *E. coli* R1 (5) and R2 (6, 7) proteins have been determined, and the mechanism of diferric-Y· cofactor assembly has been probed by a variety of spectroscopic techniques (3). By contrast, less is known about the structure and mechanism of eukaryotic class I RNRs. A structure of mouse R2 is available (8), and cofactor formation has been investigated (9, 10). However, these studies have proved more difficult because the diiron center in mouse R2 is less stable than that in *E. coli* R2 (8, 11), and the kinetics of cluster assembly are less amenable to detection of intermediates. Because eukaryotic class I RNRs have been a successful target for anticancer drugs (12, 13), further understanding of their structure, mechanism, and regulation is imperative.

An obvious choice for a eukaryotic model system is *Saccharomyces cerevisiae*, which contains four genes encoding RNR subunits. The RNR1 and RNR3 gene products, designated Y1 and Y3, correspond to the R1 protein (14). The RNR2 gene product, designated Y2, corresponds to R2 (15, 16). Both Y1 (14) and Y2 (17) are essential for mitotic viability whereas Y3 is not normally expressed, but can rescue cells deficient in Y1 (14). The fourth gene product, RNR4 or Y4, is 56% identical to Y2 and also appears to be an R2 homolog (17, 18). Several features of the Y4 sequence are intriguing. Although Y2 contains 16 critical residues conserved in almost all R2 proteins, 6 of these residues are not conserved in Y4. In particular, 3 residues known to coordinate iron in *E. coli* R2 are absent. Two histidines are replaced by tyrosines, and a glutamic acid is changed to arginine, suggesting that Y4 cannot accommodate a diiron center. In addition, Y4 lacks the N-terminal 50 residues found in Y2 and other eukaryotic R2s. Nevertheless, deletion of Y4 is lethal in some yeast strains and impairs cell growth in others (17–20), indicative of an important role in RNR function.

Initial efforts to purify and study the yeast RNR proteins were hindered by a rapid loss of enzyme activity (21, 22), but successful purification of all four subunits has been reported recently (23, 24). A key finding of the work of Nguyen *et al.* (23) is that Y4 is required to assemble the diferric-Y· cofactor in Y2. Unlike *E. coli* R2, addition of Fe(II) and O_2 is not sufficient to generate active Y2, but inclusion of Y4 yields active Y2 and detectable Y·. A Y· cannot be generated by addition of Fe(II) and O_2 to Y4 alone, consistent with the absence of iron ligands in the Y4 sequence. These data, along with the observation that Y2 and Y4 can form a complex *in vivo* (17, 23), led to the proposal that Y4 delivers iron ions to the Y2 active site by the formation of a heterodimeric complex (23), similar to that suggested for the yeast copper chaperone for superoxide dismutase (25). In this model, Y4 might then dissociate from Y2 to allow the formation of Y2 homodimers. An alternative role of Y4 proposed by Chabes *et al.* (24) is that of a molecular, rather than metallo, chaperone. In this scenario, Y4 facilitates folding of Y2, stabilizes it in a conformation needed for cofactor assembly, and remains associated for RNR activity (17, 18, 24). Recent observations, including those presented in the accompanying paper, indicate that the Y2 and Y4 homodimers can indeed convert to active heterodimers (24, 26). To help elucidate the function of Y4 and to advance our understanding of eukaryotic RNRs, we have determined the x-ray structure of the Y2Y4 heterodimer to 2.8 Å resolution.

BIOCHEMISTRY

Abbreviations: RNR, ribonucleotide reductase; R1, large subunit of ribonucleotide reductase; R2, small subunit of ribonucleotide reductase; Y·, tyrosyl radical; Y2 and Y4, small subunits RNR2 and RNR4 of yeast ribonucleotide reductase; EMTS, ethylmercurithiosalicylate.

Data deposition: Refined coordinates have been deposited in the Protein Data Bank, www.rcsb.org (PDB ID code 1JK0).

‡To whom reprint requests should be addressed. E-mail: amyr@northwestern.edu.

The publication costs of this article were defrayed in part by page charge payment. This article must therefore be hereby marked "*advertisement*" in accordance with 18 U.S.C. §1734 solely to indicate this fact.

Materials and Methods

Crystallization and Data Collection. Y4 and His_6-tagged Y2 were purified as described (23, 26). Purified Y2 was exchanged into 50 mM Tris (pH 7.8) and concentrated to 10 mg/ml in a Millipore Microcon 10 centrifugal concentrator. Purified Y4 from a 144 mg/ml stock solution was diluted to 10 mg/ml with 50 mM Tris (pH 7.8). The Y2 and Y4 protein solutions were then mixed in equal volumes and diluted with 50 mM Tris (pH 7.8) to final concentrations of 4 mg/ml. This solution was incubated overnight at 4°C before crystallization. Crystals were grown by using the sandwich drop technique, in which a drop containing 5 μl protein solution and 5 μl precipitant solution is suspended between two siliconized glass slides. The precipitant solution consisted of 100 mM acetate buffer (pH 4.9), 14% wt/vol polyethylene glycol (PEG) 4000, and 200 mM NaCl. The final pH of the mixed drop was measured to be 5.3. Long rectangular crystals of maximum dimensions 0.10 mm $\times$ 0.10 mm $\times$ 1.0 mm appeared within 3–7 days. These crystals were transferred to a cryosolution composed of the precipitant with 20% ethylene glycol for 5 min and then flash cooled in liquid nitrogen. A 2.8-Å resolution data set was collected at Stanford Synchrotron Radiation Laboratory at -160°C by using a Mar 345 imaging plate detector (NATIVE, Table 1). The crystals belong to the space group $P2_12_12_1$ with unit cell dimensions $a = 92.9$ Å, $b = 93.0$ Å, and $c = 97.4$ Å.

Isomorphous heavy atom derivatives were prepared by soaking crystals in solutions containing the precipitant supplemented with 5% glycerol and 5 mM lead(II) acetate or 1 mM ethylmercurithiosalicylate (EMTS) for 6 h, after which the crystals were transferred to the cryosolution and flash cooled in liquid nitrogen. Anomalous data were then collected at a wavelength near the x-ray absorption edge of the heavy atom. For Fe(II) soaking experiments, Y2Y4 crystals were transferred into 10-μl drops of a thoroughly degassed cryosolution of 100 mM acetate buffer (pH 5.4), 20% vol/vol ethylene glycol, 14% wt/vol PEG 4000, and 200 mM NaCl to which solid ferrous ammonium sulfate was added to a final concentration of 10 mM Fe(II). The crystals were soaked in this cryosolution for $\approx$1 min and then flash cooled in liquid nitrogen. Derivative data sets were collected at the DuPont-Northwestern-Dow Collaborative Access Team (DND-CAT) beamline at the Advanced Photon Source at -160°C by using a 2K $\times$ 2K Mar charge-coupled device (CCD) detector (PB, EMTS, FE, Table 1). All data were processed with the programs DENZO and SCALEPACK (27).

Structure Determination. Heavy atom sites for the Pb(II) and EMTS derivatives were initially determined by Patterson analysis, and additional sites were located by using the program SOLVE (28). Refinement of these sites followed by density modification and phase extension to 3.1 Å resolution with CNS (29) yielded an interpretable electron density map in which two molecules containing a number of long α helices were apparent. The molecular model was refined by iterative cycles of rigid body refinement to 3.0 Å resolution, followed by minimization, simulated annealing, and restrained B-factor refinement to 2.8 Å resolution. After each cycle, the model was rebuilt by using the

Table 1. Data collection, phasing, and refinement statistics

	NATIVE*	ANOM†	PB†	EMTS†	FE†
Data collection					
Wavelength, Å‡	0.946	1.700	0.939	1.000	1.000
Resolution range, Å	15–2.8	25–3.1	25–3.1	25–3.6	13–2.8
Unique observations	20,645	15,836	15,682	8,432	20,856
Total observations	65,155	222,390	66,218	47,522	151,906
Completeness, %	99.9 (99.8)	99.9 (99.9)	99.0 (99.9)	85.9 (85.9)	98.2 (99.8)
R_{sym}§	0.063 (0.285)	0.081 (0.279)	0.078 (0.306)	0.077 (0.169)	0.062 (0.330)
$\langle I/\text{sigma}\rangle$	8.3 (2.7)	12.7 (2.6)	7.2 (2.7)	7.4 (3.2)	10.4 (2.3)
Phasing					
Number of sites			3	2	
R_{cullis}¶			0.84	0.85	
Phasing power (anomalous)‖			0.79 (0.63)	0.74 (0.64)	
Figure of merit			0.40 (15–3.6 Å)		
Refinement					
Resolution range, Å			9–2.8		
Number of reflections			19,752		
R factor**			0.243		
R_{free}			0.296		
Number of protein, nonhydrogen atoms			4,944		
Number of nonprotein atoms			59		
rms bond length, Å			0.008		
rms bond angles, °			1.23		
Average B values, Å^2					
Main chain			45.7		
Side chain			46.5		

*Data collected at SSRL beamline 9-1.

†Data collected at the DND-CAT beamline at the APS. The NATIVE and ANOM data sets were collected from the same crystal.

‡Values in parentheses are for the highest resolution shells: 2.85–2.80 Å for NATIVE and FE, 3.15–3.10 Å for ANOM and PB, and 3.66–3.60 Å for EMTS.

§$R_{sym} = \Sigma|I_{obs} - I_{avg}|/\Sigma I_{obs}$, where the summation is over all reflections.

¶All phasing statistics from CNS. R_{cullis} = lack of closure error/isomorphous difference.

‖Phasing power = heavy atom structure factor/rms lack of closure error.

**R-factor $= \Sigma|F_{obs} - F_{calc}|/\Sigma F_{obs}$. Seven percent of the reflections were reserved for calculation of R_{free}.

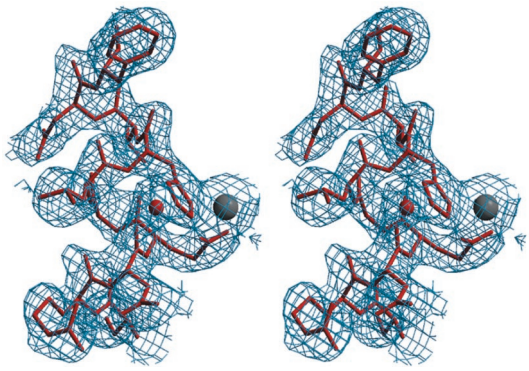

Fig. 1. Composite omit electron density map contoured at 1σ for residues 270–279 of Y2 helix αF. Two of these residues, Glu-273 and His-276, are coordinated to the zinc ion (gray sphere). A water molecule hydrogen bonded to His-276 is shown as a red sphere.

program O (30). The quality of the model was monitored by the free *R* value calculated using 7% of the data. The locations of sulfur atoms were determined from anomalous difference Fourier maps generated from anomalous scattering data collected at a wavelength of 1.7 Å (ANOM, Table 1). These sites were used to position methionine and cysteine residues in the two molecules in the asymmetric unit, and clearly showed that the asymmetric unit contained one monomer each of Y2 and Y4. In addition, the electron density for numerous side chains, including the two tyrosines in the Y4 active site region, indicated the presence of two different proteins. The final model contains a single Y2Y4 heterodimer, 58 solvent molecules, and one zinc ion (Table 1). The Y2 model includes residues 26–359, and the Y4 model includes residues 11–90, 100–263, and 275–295. No electron density was present for Y4 residues 91–99 and 264–274. A portion of a composite omit electron density map is shown in Fig. 1. Ramachandran plots generated with PROCHECK (31) show that the model exhibits good stereochemistry, with 99.7% of the Y2 residues and 98.8% of the Y4 residues in the most favored and additionally allowed regions. Accessible surface area calculations were performed with the CCP4 program AREAIMOL (32). Figures were generated with BOBSCRIPT (33), MOLSCRIPT (34), and RASTER3D (35).

Results and Discussion

Overall Structure. The Y2Y4 heterodimer is similar to the *E. coli* (6, 7) and mouse R2 (8) homodimers (Fig. 2). Both Y2 and Y4 are completely α helical and lack the β hairpins that constitute the tip of the heart shape in the *E. coli* homodimer. Y2 is composed of 13 α helices, the 8 longest of which (αA–αH) form an α helical bundle like those in *E. coli* and mouse R2. The visible portions of Y4 include 10 α helices, 8 of which (αA–αH) form the conserved 8-helix bundle structure (Figs. 2*A* and 4). No electron density is present for the C-terminal 41 residues of Y2 and 51 residues of Y4, suggesting that these regions are disordered. This observation is not surprising because the C termini are essential for interaction with the Y1 subunit (26, 36) and, in the mouse and *E. coli* systems, become structured only on complexation of the two proteins (37, 38). Although the Y4 C terminus is sensitive to proteolysis between residues 330 and 331 (26), SDS/PAGE analysis of dissolved heterodimer crystals indicates that Y4 is intact in the crystal.

A striking feature of the Y2 molecule is the presence of 3 α helices (α1–α3) at the N terminus that encompass 44 residues not observed in mouse R2 (8) (Figs. 2–4). Helix α1 interacts with αB and αG, and helix α2 interacts with αD and αG. Helix α3 is linked to αE by a hydrogen bond between Arg-66 and Glu-230. Most of this region is not conserved in Y4, but the N-terminal 10 residues in the Y4 structure form a helix that corresponds to Y2 α3. As a result of the extended Y2 N terminus, the Y2Y4 heterodimer is asymmetric. The presence of an ordered N terminus in Y2 as compared with mouse R2 can be explained by crystal packing interactions. Residues in the first 3 α helices of Y2 provide most of the crystal packing contacts. Of 15 Y2 residues involved in lattice interactions, 13 are between residues

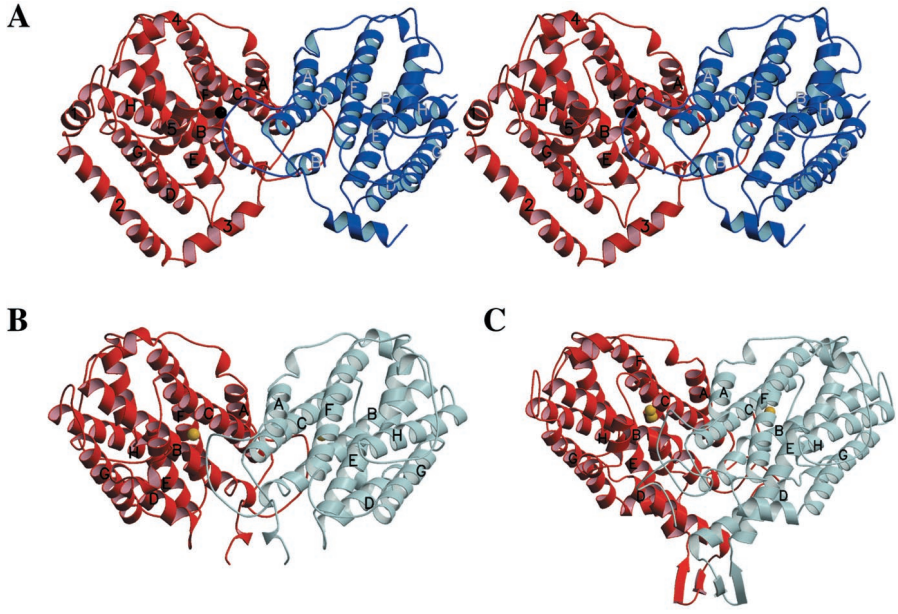

Fig. 2. Comparison of the Y2Y4 heterodimer with the mouse and *E. coli* R2 homodimers. (*A*) Stereo view of the Y2Y4 heterodimer. The Y2 molecule is shown in red and the Y4 molecule in blue. The zinc ion is shown as a gray sphere. All secondary structure elements are labeled on Y2, and the eight principal helices are labeled on Y4. (*B*) The mouse R2 homodimer (PDB accession code 1XSM). One subunit is shown in red and the other in light blue. The iron ion is shown as a yellow sphere. The eight principal helices are labeled on both subunits. (*C*) The *E. coli* R2 homodimer (PDB accession code 1RIB). One subunit is shown in red and the other in light blue. The iron ions are shown as yellow spheres. The eight principal helices are labeled on both subunits.

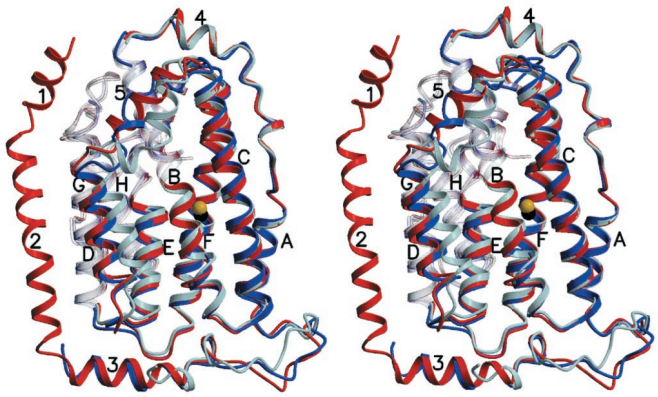

Fig. 3. Stereo superposition of Y2 (red), Y4 (blue), and mouse R2 (light blue). Secondary structure elements are labeled for Y2. Helices αA–αH are present in all three molecules and are labeled as for *E. coli* R2. The N-terminal region of αB and the C-terminal region of αE, αG, and αH are rendered transparent to emphasize helices α5 and αD. The zinc ion in Y2 is shown as a gray sphere, and the iron ion in mouse R2 is shown as a yellow sphere.

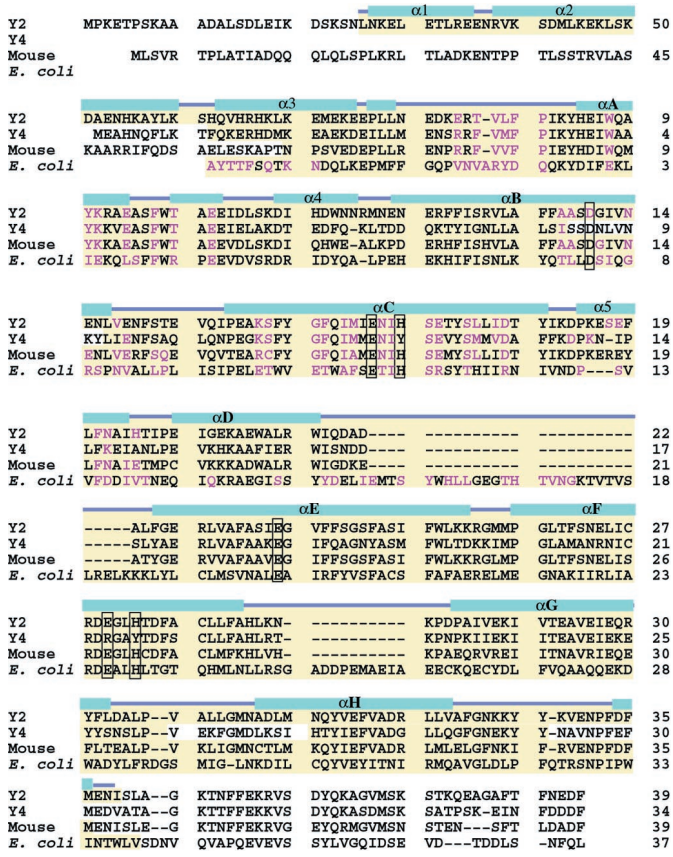

Fig. 4. Structure-based sequence alignment of Y2, Y4, mouse R2, and *E. coli* R2. The positions of the Y2 secondary structure elements are shown above the Y2 sequence. Helices are shown as thick green lines, and loops are shown as thin blue lines. Regions of the sequences present in the crystal structures are highlighted in yellow. Conserved iron ligands in Y2, mouse R2, and *E. coli* R2 and the corresponding residues in Y4 are enclosed in black boxes. Residues involved in dimer formation are shown in magenta. The accessible surface area of these residues decreases by >1 Å^2 on dimer formation.

33 and 84. By contrast, the first visible N-terminal residue in the mouse R2 structure appears to be pointed into a solvent channel.

Excluding the N terminus of Y2, Y2 and Y4 are quite similar and can be superimposed with an rms deviation of 1.2 Å for 251 Cα positions. The most significant deviation is in Y2 residues 189–207 and Y4 residues 137–157. This region in Y2 is α helical, α5, but is a loop in Y4. Notably, Y2 α5 and the following helix, αD, also differ significantly from the corresponding region in mouse R2 (Fig. 3). Compared with their positions in mouse R2, these helices are shifted by ≈5 Å toward the N-terminal helices in Y2 and away from the four-helix bundle that houses the iron binding site (αB, αC, αE, and αF). The corresponding loop and helix in Y4 are translated in the same direction. In addition, the loop connecting Y2 α3 and αA and the analogous regions in both Y4 and mouse R2 are all different from one another.

Heterodimer Interface. The Y2Y4 interface is very similar to the mouse R2 homodimer interface both in size and in specific interactions. On heterodimer formation, 2,517 Å^2 (1,223 Å^2 from Y2 and 1,294 Å^2 from Y4) accessible surface area is buried as compared with 2,698 Å^2 (1,484 Å^2 per monomer) for the mouse R2 dimer. By contrast, ≈6,000 Å^2 accessible surface area is buried on formation of the *E. coli* R2 homodimer. Many residues involved in protein–protein contacts are concentrated on helix αC in both Y2 and Y4. Additional interactions involve residues derived from αB, α5, and the loop connecting α3 and αA (Figs. 2*A* and 4). In mouse R2, Phe-102, Phe-165, and Ala-168 generate a hydrophobic cluster at the interface (8). The same cluster is present in the Y2Y4 heterodimer, formed by Phe-107, Phe-171, and Met-174 from Y2 and Phe-56, Phe-119, Met-122 from Y4. Several interactions between charged residues are also observed. Y2 Lys-101 is hydrogen bonded to Y4 Glu-60 and Y4 Glu-129, and Y4 Lys-50 is hydrogen bonded to Y2 Glu-111 and Glu-181. These two lysines correspond to mouse R2 Lys-96, which forms a number of salt bridges. Many other residues located at the heterodimer interface are conserved among Y2, Y4, mouse R2, and *E. coli* R2, although the lengthening of helices αD and αE in *E. coli* R2 render its interface significantly larger (Fig. 4). Despite these similarities, variations among Y2 α5, the loop connecting Y2 α3 and αA, and their structural counterparts in Y4 and mouse R2 render the edges of the heterodimer interface different from the edges of the mouse R2 homodimer interface. As a result, Glu-84, Thr-86, Val-87, Leu-88, and Pro-90 in Y2 and Arg-33, Phe-35, Val-36, Met-37, and Pro-39 in Y4 occupy different positions than the equivalent residues in mouse R2.

Y2 and Y4 Active Site Regions. The active site in Y2 contains all of the residues used for diiron cluster formation in *E. coli* R2 (6, 7) (Figs. 4 and 5*A*). There are two histidines, His 179 and His-276, three glutamic acids, Glu-176, Glu-239, and Glu-273, and a single aspartic acid, Asp-145. In addition, a 7σ peak in the position occupied by Fe2 in *E. coli* R2 was evident in difference Fourier maps. An anomalous difference Fourier map calculated using the ANOM data set (Table 1) showed no density at this position. Because this data set was collected at a wavelength near the iron K edge, the absence of a peak at this site suggests that the metal ion is not iron. An anomalous difference Fourier map calculated using the NATIVE data set gave a 6σ peak, however (Fig. 5*A*). The NATIVE data set was acquired at a wavelength of 0.946 Å, which is closer to the absorption edges of zinc and of numerous heavy metals. Based on the presence of this peak and the observed coordination environment, the density was modeled as a partially occupied Zn(II) ion. The zinc ion is coordinated by one side chain oxygen each from Glu-176, Glu-239, and Glu-273, and by the δ nitrogen of His-276 in a distorted tetrahedral geometry. A single bound metal ion, assigned as Fe(III), is also observed in the mouse R2 Fe2 site (8). Both His-276 and its mouse R2 counterpart are hydrogen bonded to water molecules rather than to other residues, as in *E. coli* R2 (Fig. 1). The second histidine, His-179, is properly positioned to ligate a second metal ion in the Fe1 site and is hydrogen bonded to Asp-272.

The aspartic acid, Asp-145, is not well ordered with a B-value

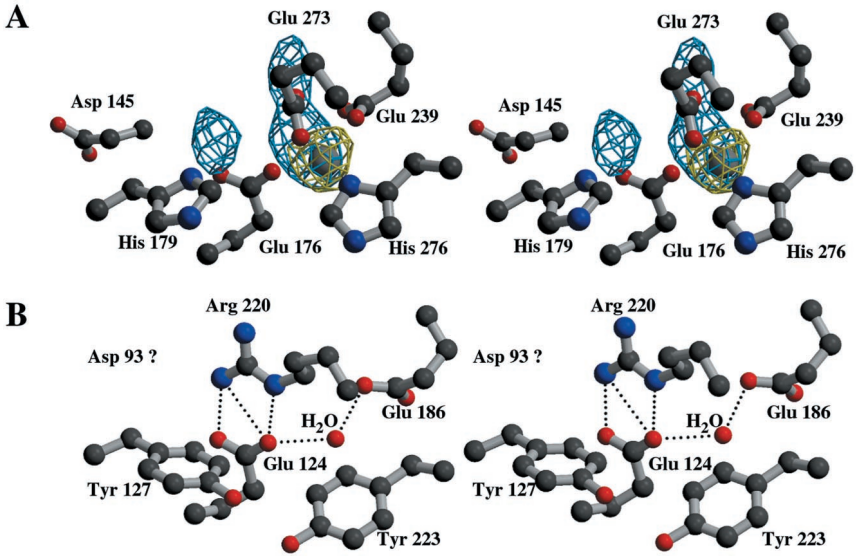

Fig. 5. Active site regions of Y2 and Y4. (*A*) Stereo view of Y2 active site region. One metal ion, assigned as Zn(II), is shown as a gray sphere. An anomalous difference Fourier map calculated using the NATIVE data set (yellow, contoured at 3.2σ) and an isomorphous difference Fourier map calculated using the FE and NATIVE data sets (blue, contoured at 6σ) are superimposed. (*B*) Stereo view of the Y4 active site regions. Key hydrogen bonding interactions are denoted with dotted lines. Asp-93 is not visible in the electron density map.

of ≈80 Å^2, and was best modeled as pointing away from the Fe1 site. In this position, one of its side chain oxygens is within hydrogen bonding distance of a water molecule. By contrast, the analogous aspartic acid in mouse R2 points toward the Fe1 site, although it is farther away than the same residue in *E. coli* R2. Because the crystals were grown at pH 5.3 and frozen at pH 4.9, different protonation states could account for the apparent flexibility of Asp-145. Residues 146–148 are also disordered, suggesting that occupation of the Fe1 site might be required to order this region. The expected site of Y· formation, Tyr-183, occupies the same position as in the other R2s. The combination of the Asp-145 conformation and the shifted position of helix αD renders the Y2 active site even more exposed than the mouse R2 active site (8).

Three of the 6 Y2 active site residues are conserved in Y4, two glutamic acids and the aspartic acid (Fig. 5*B*). Both Glu-124 and Glu-186 occupy positions similar to those of their Y2 counterparts. A water molecule not observed in Y2 links Glu-186 to Glu-124 and Gln-120. The aspartic acid, Asp-93, and surrounding residues 91–99 are not visible in the electron density map and could not be modeled. Two tyrosines, Tyr-127 and Tyr-223, replace the two histidines in the Y2 active site. The side chain oxygen atoms of these two tyrosines are separated by 3 Å, and the side chain oxygen of Tyr-127 is hydrogen bonded to the side chain of Asp-219. Perhaps the most unusual feature of the Y4 active site region is the presence of an arginine, Arg-220. One Arg-220 η nitrogen is hydrogen bonded to both side chain oxygens of Glu-124, one of which also interacts with the Arg-220 ε nitrogen. The other η nitrogen is ≈2.5 Å from the side chain oxygen of Tyr-194 and ≈3.5 Å from the side chain of Gln-190. These 2 residues, along with Asn-193, Tyr-127, Tyr-223, and Arg-220, constitute the 6 of 16 critical eukaryotic R2 residues not conserved in Y4. The identities and positions of the Y4 active site residues strongly suggest that this site does not bind iron. Moreover, no extra electron density attributable to a metal ion is observed.

To further probe the iron binding capabilities of both Y2 and Y4, heterodimer crystals were treated with ferrous ammonium sulfate at pH 5.1. The soaking time had to be limited to 1 min to preserve diffraction quality. A 2.8-Å resolution isomorphous difference Fourier map calculated using the FE and NATIVE data sets revealed two peaks at the Y2 iron binding site: a 15σ peak at the Fe2 site and a 10σ peak at the Fe1 site (Fig. 5*A*). No significant peaks were observed in the Y4 active site region or anywhere else in the Y4 molecule, confirming that Y4 does not bind iron under these conditions. The peaks in Y2 are 3.7 Å apart, a distance similar to the Fe···Fe separation in reduced wild-type *E. coli* R2 (39). The presence of these two peaks demonstrates that Y2 can accommodate a diiron center. There are several possible explanations for the lower intensity of the Fe1 peak. First, the low pH of the crystallization (5.3) and soaking (5.1) solutions could preclude proper assembly of the diiron center. Alternatively, a longer soak time might be necessary to fill the Fe1 site. Finally, the putative zinc ion already present at Fe2 in some fraction of the molecules might prevent binding at Fe1 in these molecules. Removal of this metal ion could be necessary to properly assemble the diiron cluster. Additional difference electron density observed near the Fe2 site (Fig. 5*A*) is not consistent with a shift of either Glu-239 or Glu-273, but instead corresponds to a site occupied by exogenous ligands in mutants of *E. coli* R2. A solvent molecule occupies this site in the reduced D84E mutant (40), and azide is bound at this position in the F208A/Y122F double mutant (41). It therefore seems likely that an exogenous ligand is present in the iron-treated Y2 crystals. A possible candidate for this ligand is acetate ion because acetate is present in high concentrations in the crystal soaking solution.

Function of Y4. Two possible roles for Y4 have been proposed based on its initial characterization. First, Y4 could act catalytically as a metallochaperone, delivering iron ions to Y2 via a transient heterodimeric complex (23). The inability to detect ferric or ferrous iron binding to Y4 and the isolation (26) and crystallization of a stable Y2Y4 heterodimer starting with the two homodimers are not consistent with this function. In addition, activity assays demonstrate that Y4 activates Y2 stoichiometrically rather than catalytically (24, 26), and quantitative Western analysis shows that the two proteins are present in comparable amounts in yeast cells (26), although their localization and concentration as a function of cell cycle have yet to be determined. Finally, deletion of the Y4 C-terminal tail, initially proposed to bind iron (23), does not interfere with iron loading of Y2 *in vitro* (24, 26). It therefore seems unlikely that Y4 binds iron and delivers it directly to the Y2 active site.

The second proposed role of Y4 is that of a molecular chaperone, facilitating folding of Y2 (24). Because the His_6-tagged Y2 is amenable to purification, folded according to CD spectroscopy (26), and well behaved in crystallization trials, Y4 does not appear to be essential for proper folding of this His_6-tagged form of Y2. It is possible, however, that Y4 stabilizes

Y2 in the proper conformation for iron cluster assembly and Y· formation. Even if Y4 does not directly insert iron into Y2, it could promote interaction with another assembly protein or simply hold Y2 in a position that renders the active site more accessible to ferrous iron delivered by another protein or transporter. If this is the only function of Y4, the two proteins might be expected to dissociate after the diferric-Y· cofactor is generated. It is not yet known whether Y2 can form active homodimers once the cofactor is assembled.

If the heterodimer does dissociate after cofactor assembly, iron loading of Y2 might modulate the affinity of Y2 for Y4. For example, the conformation of Asp-145 is expected to change on iron binding. A shift of this residue toward the diiron center could propagate changes in the adjacent helix αC, which houses numerous residues involved in the heterodimer interface. In particular, Lys-166 on helix αC is predicted to be near Y4 Lys-98, which is disordered in the present structure. It is conceivable that iron binding brings these two lysines closer together, increasing electrostatic repulsion and facilitating dissociation of the heterodimer. Because the corresponding residue in Y2 and also in mouse R2 is a glutamic acid (Fig. 4), a similar unfavorable interaction would not occur in the Y2 homodimer.

The presence of comparable amounts of Y2 and Y4 in yeast cells and the detection of 0.6–0.8 Y· per heterodimer (26) suggest that the heterodimer might remain intact, however. If the heterodimer is the active species *in vivo*, Y4 probably not only assists in cofactor assembly, but also stabilizes Y2 in an active conformation. By analogy to the *E. coli* system (5), the Y2Y4 heterodimer would then interact with the Y1 homodimer. It is unclear why such a complex between heterodimer and homodimer would be necessary or advantageous. Structural characterization of both the activated heterodimer and the Y2 homodimer, combined with further biochemical and *in vivo* studies, should clarify the exact role of Y4 in DNA synthesis.

This work was supported by National Institutes of Health (NIH) Grants GM58518 (A.C.R.) and GM29595 (J.S.). W.C.V. is supported in part by NIH Training Grant GM08382. The DuPont-Northwestern-Dow Collaborative Access Team (DND-CAT) Synchrotron Research Center at the Advanced Photon Source (APS) is supported by the E. I. DuPont de Nemours & Co., the Dow Chemical Company, the National Science Foundation, and the State of Illinois. The Stanford Synchrotron Radiation Laboratory (SSRL) is funded by the Department of Energy (Basic Energy Sciences and Biological and Environmental Research) and NIH (National Center for Research Resources and National Institute of General Medical Sciences).

1. Reichard, P. (1993) *Science* **260,** 1773–1777.
2. Sjöberg, B.-M. (1997) *Struct. Bonding* **88,** 139–173.
3. Stubbe, J. & Riggs-Gelasco, P. (1998) *Trends Biochem. Sci.* **23,** 438–443.
4. Stubbe, J. & van der Donk, W. A. (1998) *Chem. Rev.* **98,** 705–762.
5. Uhlin, U. & Eklund, H. (1994) *Nature (London)* **370,** 533–539.
6. Nordlund, P., Sjöberg, B.-M. & Eklund, H. (1990) *Nature (London)* **345,** 593–598.
7. Nordlund, P. & Eklund, H. (1993) *J. Mol. Biol.* **231,** 123–164.
8. Kauppi, B., Nielsen, B. B., Ramaswamy, S., Larsen, I. K., Thelander, M., Thelander, L. & Eklund, H. (1996) *J. Mol. Biol.* **262,** 706–720.
9. Schmidt, P. P., Rova, U., Katterle, B., Thelander, L. & Gräslund, A. (1998) *J. Biol. Chem.* **273,** 21463–21472.
10. Pötsch, S., Lendzian, F., Ingermarson, R., Hörnberg, A., Thelander, L., Lubitz, W., Lassmann, G. & Gräslund, A. (1999) *J. Biol. Chem.* **274,** 17696–17704.
11. Nyholm, S., Thelander, L. & Gräslund, A. (1993) *Biochemistry* **32,** 11569–11574.
12. Heinemann, V. (2001) *Oncology* **60,** 8–18.
13. Gwilt, P. R. & Tracewell, W. G. (1998) *Clin. Pharmacokinet.* **34,** 347–358.
14. Elledge, S. J. & Davis, R. W. (1990) *Genes Dev.* **4,** 740–751.
15. Elledge, S. J. & Davis, R. W. (1987) *Mol. Cell. Biol.* **7,** 2783–2793.
16. Hurd, H. K., Roberts, C. W. & Roberts, J. W. (1987) *Mol. Cell. Biol.* **7,** 3673–3677.
17. Huang, M. & Elledge, S. J. (1997) *Mol. Cell. Biol.* **17,** 6105–6113.
18. Wang, P. J., Chabes, A., Casagrande, R., Tian, X. C., Thelander, L. & Huffaker, T. C. (1997) *Mol. Cell. Biol.* **17,** 6114–6121.
19. Winzeler, E. A., Shoemaker, D. D., Astromoff, A., Liang, H., Anderson, K., Andre, B., Bangham, R., Benito, R., Boeke, J. D., Bussey, H., *et al*. (1999) *Science* **285,** 901–906.
20. Kumar, A., Cheung, K.-H., Ross-Macdonald, P., Coelho, P. S. R., Miller, P. & Snyder, M. (2000) *Nucleic Acids Res.* **28,** 81–84.
21. Lammers, M. & Follmann, H. (1984) *Eur. J. Biochem.* **140,** 281–287.
22. Harder, J. & Follmann, H. (1990) *Free Radical Res. Commun.* **19,** 281–286.
23. Nguyen, H.-H. T., Ge, J., Perlstein, D. L. & Stubbe, J. (1999) *Proc. Natl. Acad. Sci. USA* **96,** 12339–12344.
24. Chabes, A., Domkin, V., Larsson, G., Liu, A., Gräslund, A., Wijmenga, S. & Thelander, L. (2000) *Proc. Natl. Acad. Sci. USA* **97,** 2474–2479.
25. Lamb, A. L., Torres, A. S., O'Halloran, T. V. & Rosenzweig, A. C. (2000) *Biochemistry* **39,** 14720–14727.
26. Ge, J., Perlstein, D. L., Nguyen, H.-H., Bar, G., Griffin, R. G. & Stubbe, J. (2001) *Proc. Natl. Acad. Sci. USA* **98,** 10067–10072.
27. Otwinowski, Z. & Minor, W. (1997) *Methods Enzymol.* **276,** 307–326.
28. Terwilliger, T. C. & Berendzen, J. (1999) *Acta Crystallogr. D* **55,** 849–861.
29. Brünger, A. T., Adams, P. D., Clore, G. M., DeLano, W. L., Gros, P., Grosse-Kunstleve, R. W., Jiang, J.-S., Kuszewski, J., Nilges, M., Pannu, N. S., *et al*. (1998) *Acta Crystallogr. D* **54,** 905–921.
30. Jones, T. A., Zou, J.-Y., Cowan, S. W. & Kjeldgaard, M. (1991) *Acta Crystallogr. A* **47,** 110–119.
31. Laskowski, R. A. (1993) *J. Appl. Crystallogr.* **26,** 283–291.
32. Collaborative Computational Project (1994) *Acta Crystallogr. D* **50,** 760–763.
33. Esnouf, R. M. (1997) *J. Mol. Graph. Model.* **15,** 132–134.
34. Kraulis, P. J. (1991) *J. Appl. Crystallogr.* **24,** 946–950.
35. Merritt, E. A. & Bacon, D. J. (1997) *Methods Enzymol.* **277,** 505–524.
36. Fisher, A., Yang, F. D., Rubin, H. & Cooperman, B. S. (1993) *J. Med. Chem.* **36,** 3859–3862.
37. Lycksell, P. O., Ingemarson, R., Davis, R., Gräslund, A. & Thelander, L. (1994) *Biochemistry* **33,** 2838–2842.
38. Lycksell, P. O. & Sahlin, M. (1995) *FEBS Lett.* **368,** 441–444.
39. Logan, D. T., Su, X.-D., Åberg, A., Regnström, K., Hajdu, J., Eklund, H. & Nordlund, P. (1996) *Structure* **4,** 1053–1064.
40. Voegtli, W. C., Khidekel, N., Baldwin, J., Ley, B. A., Bollinger, J. M., Jr., & Rosenzweig, A. C. (2000) *J. Am. Chem. Soc.* **122,** 3255–3261.
41. Andersson, M. E., Högbom, M., Rinaldo-Matthis, A., Andersson, K. K., Sjöberg, B.-M. & Nordlund, P. (1999) *J. Am. Chem. Soc.* **121,** 2346–2352.